ORIGINAL PAPER

Surface yttrium-doping induced by element segregation to suppress oxygen release in Li-rich layered oxide cathodes

Si-Yu Liu[1,2] · Yu-Huan Zhou[1,3] · Yi-Bin Zhang[1,4] · Sheng-Jie Xia[1] · Ying Li[1,5] · Xin Zhou[1,3] · Bao Qiu[1] · Guang-Jie Shao[2] · Zhao-Ping Liu[1]

Abstract

Doping electrochemically inert elements in Li-rich layered oxide cathodes usually stabilizes the structure to improve electrochemical performance at the expense of available capacity. Here, we use an element segregation principle to realize a uniform surface doping without capacity sacrifice. On the basis of Hume-Rothery rule, element yttrium is chosen as a candidate dopant to spontaneously segregate at particle surface due to mismatched ionic size. Combined with X-ray photoelectron spectroscopy and electron energy loss spectroscopy mapping, yttrium is demonstrated uniformly distributed on particle surface. More importantly, a significant alleviation of oxygen release after surface doping is detected by operando differential electrochemical mass spectrometry. As a result, the modified sample exhibits improved reversibility of oxygen redox with 82.1% coulombic efficiency and excellent cycle performances with 84.15% capacity retention after 140 cycles. Postmortem analysis by transmission electron microscopy, Raman spectroscopy and X-ray diffraction reveal that the modified sample maintains the layered structure without a significant structure transformation after long cycles. This work provides an effective strategy with a series of elements to meet the industrial application.

Keywords Li-ion batteries · Cathode materials · Li-rich layered oxides · Surface doping

Si-Yu Liu and Yu-Huan Zhou have contributed equally to this work.

✉ Bao Qiu
  qiubao@nimte.ac.cn

✉ Guang-Jie Shao
  shaogj@ysu.edu.cn

✉ Zhao-Ping Liu
  liuzp@nimte.ac.cn

1   Ningbo Institute of Materials Technology and Engineering, Chinese Academy of Sciences, Ningbo 315201, China

2   College of Environmental and Chemical Engineering, State Key Laboratory of Metastable Materials Science and Technology, Yanshan University, Qinhuangdao 066004, China

3   University of Chinese Academy of Sciences, Beijing 100049, China

4   Science and Chemical Engineering, Ningbo University, Ningbo 315211, China

5   College of Chemical Engineering, Zhejiang University of Technology, Hangzhou 310014, China

1 Introduction

In order to develop large energy storage devices and electric vehicles, energy density of lithium ion batteries (LIBs) needs to be improved. The key to increase the energy density depends on the specific capacity of cathode materials [1, 2]. Li-rich layered oxide cathodes (LLOs) with a formula of $x\mathrm{Li_2MnO_3}\cdot(1-x)\mathrm{LiMO_2}$ (M = Co, Ni, Mn) are considered as promising cathode materials for LIBs due to their advantages of ultrahigh specific capacity and low cost price. The large capacity of LLOs comes from accumulation of lattice oxygen redox and transition metal redox [3]. The oxygen redox is now identified as one of the most effective ways to conquer the capacity limitation of conventional transition metal redox centers [4, 5]. However, a significantly irreversible oxygen release happens during the oxygen redox activation in the initial charge. The problem triggers some application puzzle concerning safety, battery performance and battery calendar life [6–8]. An urgent demand that solves the oxygen release problem is proposed for commercialization of LLOs.

The earliest investigation of the oxygen release can be traced back to 2002. Dahn's group [9] first proposed the concept of irreversible oxygen loss. Oxygen release is found to start from the activation plateau about voltage at 4.5 V during the initial charge process. Bruce [10] first detected the formation of O_2 gas during the initial charge via differential electrochemical mass spectrometry (DEMS). It is subsequently demonstrated through ^{18}O isotopic tracer that the O_2 gas is originated from LLOs lattice oxygen, generating oxygen vacancies on particle surface [11]. During the extended cycles, the oxygen vacancies are continuously pumped into bulk lattice, which is driven by oxygen redox, eventually causing structure decomposition and electrochemical degradation [12–14]. The understanding enlightens surface modifications as a suitable way to suppress the oxygen release to circumvent the situation, which mainly includes coating, doping and surface pretreatment etc. Among all of them, surface doping is one of the most effective approaches to achieve the surface modification. Generally, the modification stabilizes the surface oxygen based on M–O bonding (M = dopants). Elements with a strong binding energy with oxygen are the preferred dopants, such as B [15], Nb [16], V [17] and La [18].

While many methods can be used to achieve the surface doping, an annealing process is essential as the last step to make the dopant bond with the surface oxygen. However, the heat treatment also provides a diffusion energy to enable the dopant invade into bulk lattice and substitute host cations [19]. As a consequence, the injection of the dopant would induce an inhomogeneous surface doping and capacity reduction. Therefore, it is important to control the doping depth and prevent the bulk diffusion. A rule named as Hume-Rothery tells that a solid solubility is negligible when a size misfit between the solvent and solute atoms exceeds 15%. The rule suggests that large size differences between host elements and doping elements can be a driven force to make the doping elements dissolve out from the host structure [20–22]. The rule is embodied in the previous studies, such as yttrium-doped ZrO_2 and titanium-doped Al_2O_3 in some ceramic materials [22, 23]. For Li-ion batteries, it is reported that tungsten (W) is doped on the surface of $LiNiO_2$ material, which does not substitute Ni or Li in the $LiNiO_2$ lattice no matter how it is added at the precursor synthesis stage [24]. In that case, pure surface doping without bulk diffusion can be realized based on the incompatibility between the dopant and the host. A series of transition metal elements could be suitable for the doping strategy, considering the ionic size and bonding energy (shown in Fig. 1).

Based on above consideration, element yttrium (Y) is used as a dopant to achieve surface doping on Li-rich layered oxide cathode $Li_{1.2}Ni_{0.13}Co_{0.13}Mn_{0.54}O_2$. Compared to the host cations of the Li-rich layered oxides, Y element owes large ionic size ($r(Y^{3+}) = 0.104$ nm, $r(Ni^{2+}) = 0.069$ nm, $r(Co^{3+}) = 0.0685$ nm, $r(Mn^{4+}) = 0.053$ nm and $r(Li^+) = 0.076$ nm). Besides, the bond strength of Y–O reaches 714.1 ± 10.2 kJ·mol^{-1}, which is strong enough to prevent the surface O from escaping [25, 26]. X-ray photoelectron spectroscopy (XPS) and electron energy loss spectroscopy (EELS) reveal that the Y segregated at surface of grain particles. O_2 evolution of the initial cycle is monitored by operando differential electrochemical mass spectroscopy (DEMS) measurement. Postmortem analysis by multiscale characterizations revealed that the Y-doped sample exhibits better structural integrity and less electrochemical impedance after cycling.

Fig. 1 Surface doping of elements induced by element segregation
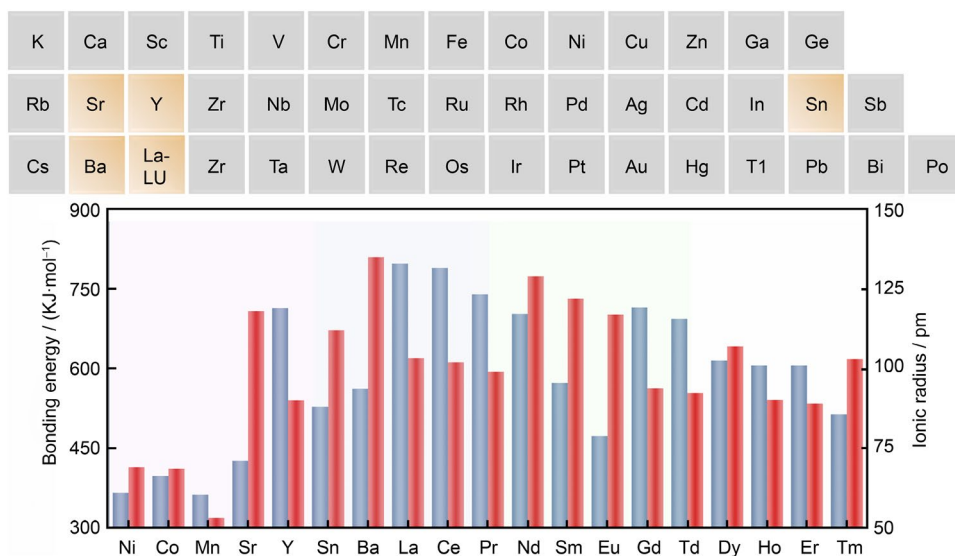
2 Experimental

2.1 Materials synthesis

$Li_{1.2}Ni_{0.13}Co_{0.13}Mn_{0.54}O_2$ (LLO114) and a series of Y-doped LLO114 cathode materials were synthesized by the solid-phase method. $C_4H_6NiO_4 \cdot 4H_2O$, $C_4H_6CoO_4 \cdot 4H_2O$, $MnC_4H_6O_4 \cdot 4H_2O$ (Sinopharm Chemical Reagent Co., Ltd., Shanghai, China) and oxalate precipitator were mixed by a molar ratio of 1:1:4:1. The Li_2CO_3 was then mixed according to the molar ratio of Li:transition metals = 1:1.5. The agate beads were weighed by the mass ratio of 1:1 with the total materials. A planetary activator was running at 500 r·min^{-1} to evenly mix the powders. The mixed powders were calcined at 500 °C for 5 h and at 850 °C for 12 h in an air atmosphere, using a heating ramp of 5 °C·min^{-1}.

For preparing surface Y doped $Li_{1.2}Ni_{0.13}Co_{0.13}Mn_{0.54}O_2$, first, the $C_4H_6NiO_4 \cdot 4H_2O$, $C_4H_6CoO_4 \cdot 4H_2O$, $MnC_4H_6O_4 \cdot 4H_2O$ (Sinopharm Chemical Reagent Co., Ltd., Shanghai, China), oxalate precipitator and $YN_3O_9 \cdot 6H_2O$ were mixed in a molar ratio of 1:1:4:1:0.005, 0.01, 0.03, 0.07. The next steps were the same as the previous preparations for LLO114. The final products were abbreviated as LLO114-Y0.5, LLO114-Y1, LLO114-Y3 and LLO114-Y7, respectively.

2.2 Materials characterization

X-ray diffraction (XRD, Bruker, D8 Advance Davinci) was applied to analyse long-range structural of the cathodes. XPS (Kratos, Axis Supra) was performed to observe the surface element ingredient. Inductively coupled plasma optical emission spectrometry (ICP-OES, Spectro, Spectro Arcos) was performed as the elemental analysis. A field emission scanning electron microscope (SEM, Hitachi, S4800) was utilized to observe the morphology of materials. DEMS (Linglu Instrument Co. Ltd., Shanghai, China) was used to monitor the gas production of materials. The required cathode mass load for DEMS was approximately 21 mg·cm^{-2}. Raman spectrometer (Raman, Renishaw, Renishaw inVia Reflex) was used to observe the local structure with a 530-nm excitation laser source. High-resolution lattice fringe images and EELS mapping were carried out via transmission electron microscope (TF20, FEI, Tecnai F20).

2.3 Electrochemical measurement

Electrode slurries were produced by mixing active material, super P carbon and polyvinylidene fluoride (PVDF) binder through a homogenizer in a mass ratio of 8:1:1. After mixing, the slurries were coated on aluminum foils and dried at 80 °C for 10 h in an oven. The electrochemical tests were executed by assembling 2032 coin half cells, which consists of cathode electrodes, Celgard 2502 membrane as a separator and Li metal as an anode. The electrolyte was made up of ethylene and dimethyl carbonate (3:7 vol ratio) with $LiPF_6$ (1.0 M). Galvanostatic charge–discharge was taken to cycle the cells in 2.0–4.8 V vs. Li^+/Li^0 at 25 °C on a LAND-CT2001A battery test system. The current density of 1.0 C corresponds to 250 mA·g^{-1}. Galvanostatic intermittent titration technique (GITT) experiment were carried out on a LAND-CT2001A battery system with 1 h pulse and 2 h rest. The pulse current density was 0.05 C. The electrochemical impedance spectroscopy (EIS) was measured in the frequency range of 10^5–10^{-2} Hz (Autolab83710 impedance analyser).

3 Results and discussion

3.1 Characterizations of the pristine samples

The LLO114 and a series of Y-doped LLO114 samples are synthesized by solid-state method. In order to seek the optimal Y-doping amount, various compositions of Y-doped LLO114 samples were prepared by changing Y content from 0.5 at.% to 7 at.%. The electrochemical performances of the LLO114 and a series of Y-doped LLO114 samples at 0.1 C are illustrated in Fig. S1. The sample with 3 at.% Y content (LLO114-Y3) shows the best performance, which is considered as the optimal doping amount. Therefore, it is used as modified sample to compare with the pristine sample to study the effect of Y doping and then is called LLO114-Y for short. The chemical compositions of LLO114 and LLO114-Y samples certified by ICP-OES are labeled in Table S1, presenting nearly the same composition except the doped Y. The content of Y in doped sample is about 2.7 at.%, consisting with the designed composition. Fig. S2 shows SEM images of the LLO114 and the LLO114-Y. No difference can be observed from the images, indicating that Y doping has no influence on morphology.

As shown in Fig. 2a, b, all diffraction peaks of both samples can be indexed as α-NaFeO$_2$ phase, which is a layered structure with alkaline metals (Li layer) and transition metals (TM layer) alternatively occupy cubic-close-packing oxygen octahedral. Extra peaks emerging at 20~25° can be explained by regionally enriched LiTM$_6$ ordered arrangement in TM layer, suggesting existence of Li_2MnO_3 phase. The results show that both of the as-prepared samples occupy a typical Li-rich layered structure as previous reports in the samples [27, 28]. Rietveld refinement is used to fit the experiment patterns using a layered model (Space group: R-3 m Table S2). Good fittings are achieved with R-weighted pattern (R_{wp}) 5.70% for LLO114 and 6.58% for LLO114-Y,
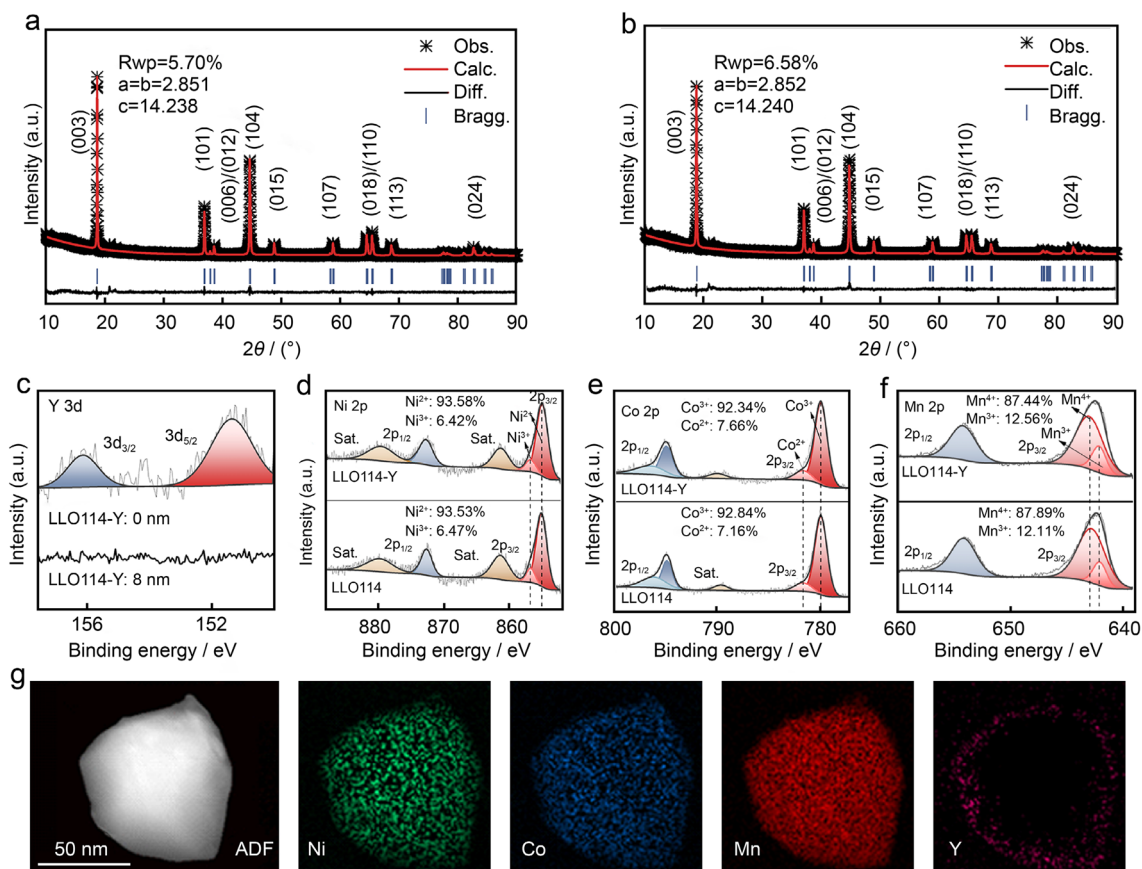
Fig. 2 a, **b** XRD patterns and single-phase refinement patterns for LLO114 and LLO114-Y, respectively; **c** XPS results of Y 3d for LLO114-Y by etching; **d**–**f** Experimental and fitting results of XPS for Ni 2p, Co 2p and Mn 2p in LLO114 and LLO114-Y; **g** STEM-EELS spectrum images for the LLO114-Y. Scale bar, 50 nm

respectively. Lattice parameters of LLO114-Y is almost keep the same as unmodified LLO114. Besides, adding Y to Li site or TM site does not promote the intensity fitting (Fig. S3). The results indicate that Y doping has no impact on the bulk structure of LLO114.

To further detect the distribution of Y, surface-sensitive XPS is performed. Figure 2c shows two peaks at around 151.8 eV and 155.9 eV, indicating existence of Y^{3+} on particle surface [29]. After etching, the signal of Y disappears, suggesting that Y does not enter into particle. Figure 2d–f compares the valence state of Ni, Co and Mn for LLO114-Y and bare LLO114 by peak fitting [30–35]. The fitting exhibits that Ni, Co and Mn of both samples have almost the same peak area ratios and binding energy. The XPS results show that introducing Y^{3+} into lattice does not change the chemical valence states of LLO114. Scanning transmission electron microscopy electron energy loss spectroscopy (STEM-EELS) mapping is carried out to directly investigate the spatial distribution of each element for single grain. As shown in Fig. 2g and Fig. S4, Ni, Co and Mn element for two samples exhibit a homogenous distribution, but the element

Y for LLO114-Y is enriched at particle surface, consisting with XPS results. The above analysis demonstrates that the as-prepared LLO114 and LLO114-Y possess a typical Li-rich layered structure. Element Y is not incorporated into the bulk of structure even if it is evenly mixed with other elements before calcination. In contrast, it segregates out at particle surface.

3.2 Gas evolution monitor

To evaluate the effect of surface Y doping on the oxygen release in LLOs, operando gas monitoring of the two samples was taken via DEMS. As shown in Fig. 3, no obvious CO_2 or O_2 release can be detected in the voltage regime less than 4.5 V. With the charge to the plateau region of oxygen activation, a significant CO_2 gas can be detected on both sample, but Y-doped LLO114 exhibits less CO_2 generation. Previous study has revealed that the CO_2 gas is mainly originated from decomposition of organic electrolyte solvent on the cathode side [36, 37]. The less CO_2 generation on LLO114-Y might be related to surface Y covering layer. For
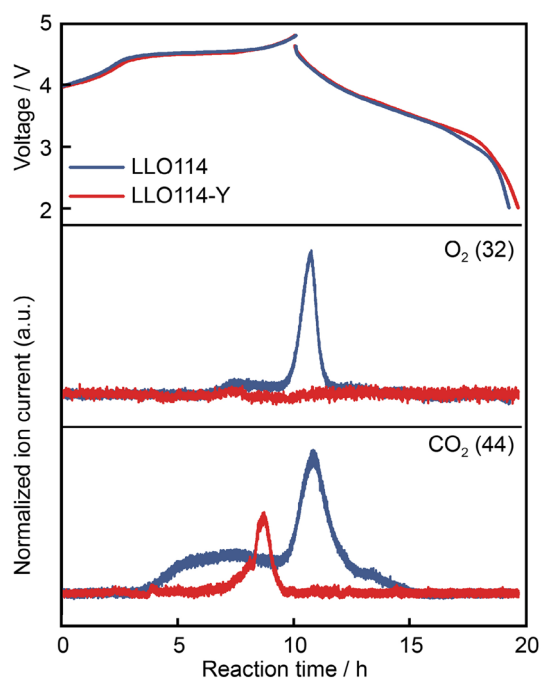
Fig. 3 The initial charge–discharge curves of LLO114 and LLO114-Y with O_2 and CO_2 release rates as detacted by DEMS. The in-situ cells were cycled at 0.1 °C from 2.0 to 4.8 V

O_2 evolution, the oxygen release mainly occurs at the end of the charge, as dramatic O_2 peak is detected on LLO114 above 4.6 V. Nevertheless, Y-doped sample exhibits little oxygen release in the whole cycle, indicating that surface Y doping can effectively suppress the oxygen release. It is believed that the suppressed oxygen release facilitates better electrochemical performances and structure stability [38].

### 3.3 Electrochemical performance measurements

Figure 4a shows the initial charge/dishcharge profiles of LLO114 and LLO114-Y from 2.0 to 4.8 V at 0.1 °C. Both of the samples exhibit the staircase charge profiles and S-shape discharge profiles. The charge capacity of LLO114-Y is slightly lower than that of LLO114, while the discharge capacity of LLO114-Y is slightly higher than LLO114. Figure 4b shows the capacity contributions of the initial cycle from different voltage regions. Compared with the two samples, the capacities from transition metal redox (TMR) in slope region (< 4.5 V) are keep the same. The capacities from lattice oxygen redox (LOR) in plateau region (> 4.5 V) are different. LLO114-Y delivers a plateau capacity of 208.1 mAh·g^{-1} lower than LLO114 (212.2 mAh·g^{-1}). The reduced capacity is mainly from voltage region above 4.5 V, which involves in irreversible oxygen activation. The Coulomb efficiency of LLO114-Y sample is higher (82.1%) than LLO114 (77.9%). The results show that an irreversible

capacity loss in the initial cycle is suppressed for LLO114-Y. Cyclic voltammetry measurement is taken to investigate the initial activation of the electrodes. As shown in Fig. S5, two oxidation peaks emerge at 4.1 V and above 4.5 V for both cathodes, respectively. The 4.1 V peak is attributed to the Li$^+$ extraction from lattice and the concomitant oxidation of the Ni and Co ion. The 4.5-V peak represents oxygen oxidation, which specifically includes both reversible and irreversible lattice oxygen oxidation. For reduction process, the main reduction peak presents at about 3.6 V, which incorporates into a hybrid cationic and anionic contribution. The peak for LLO114-Y is slightly stronger than that of the bare LLO114. The results indicate that the oxygen redox of LLO114-Y is more reversible, which is consistent with the charge/discharge profiles. Surface Y doping can act as a stabilizer to suppress the oxygen release and alleviate the irreversible capacity loss. Figure 4c presents cycle performance of LLO114 and LLO114-Y at 0.5 °C after three activation cycles at 0.1 °C. After 140 cycles, LLO114-Y sample shows better cycle performance with 84.15% capacity retention, while the LLO114 sample exhibits rapid capacity fading from 191.8 to 129.1 mAh·g^{-1} after 140 cycles (capacity retention = 67.31%). The coulombic efficiency of LLO114-Y sample is 95.7%, while LLO114 sample is 94.5%. The rate capacities of the two samples are displayed in Fig. 4d with different current densities ranging from 0.1 to 10 °C. The specific discharge capacity of LLO114-Y sample is slightly higher than that of LLO114 sample at the low rate of 0.1 °C and 0.2 °C. With increased current densities at 0.5–10 °C, the differences become significant. The LLO114-Y shows much better rate performances than that of LLO114. Figure 4e, f shows the charge–discharge profiles of both samples upon cycling. LLO114-Y exhibits less variation on the profile shapes than that of LLO114, suggesting a suppressed voltage decay of LLO114-Y. Specifically, the average discharge voltage decay of LLO114 sample is 2.8 mV per cycle between the first and the 140th cycles, while the voltage decay of LLO114-Y is suppressed in the whole cycling (2.5 mV per cycle).

3.4 Structure charaterization after cycling

Postmortem analysis of both samples is taken to investigate structure changes after 140 cycles. Figure 5a–d presents STEM-EELS line scan from surface to bulk after 140 cycles. The O pre-peak disappeared and the O–K-edge widened in surface in LLO114 sample, while the intensity of these two peaks of LLO114-Y sample decreased slightly but the peak shape was still sharp. In addition, the O pre-peak intensity of LLO114 samples decreases in subsurface. The reduced ratio of the O–K-edge pre-peak intensities is attributed to a change in the local environment of oxygen, especially from the oxygen defect formed

Fig. 4 **a** Initial charge–discharge curves of LLO114 and LLO114-Y; **b** charge capacity and coulomb efficiency distribution of LLO114 and LLO114-Y; **c** cycling performance (down) and coulombic efficiency (up) of LLO114 and LLO114-Y during cycling at 0.5 °C; **d** discharge capacities of LLO114 and LLO114-Y at different charge/discharge rates; Selected charge/discharge voltage profiles of the **e** LLO114 and **f** LLO114-Y samples at 0.5 °C
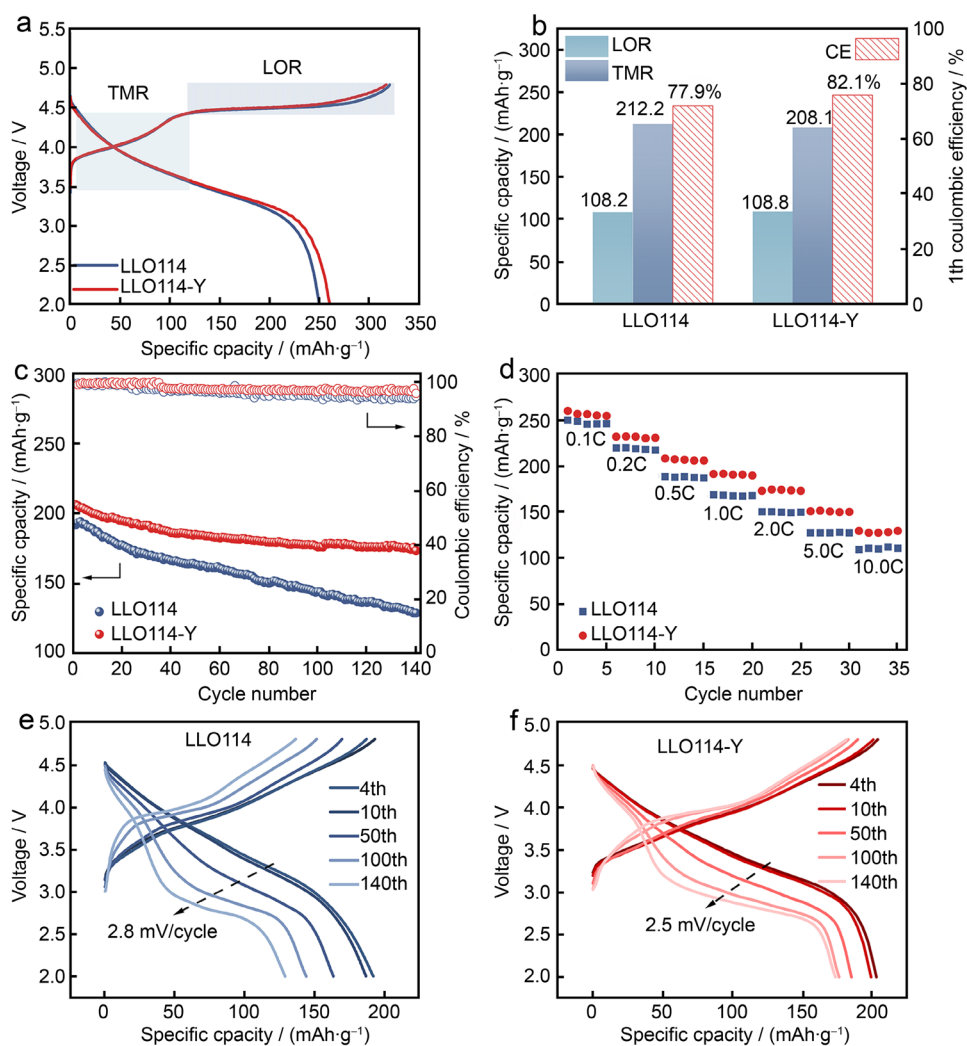
on the surface [39]. On the other hand, the L edge of Mn of LLO114 sample moves slightly to a lower value at near the surface, which indicates that the valence state of Mn decreases to compensate for the loss of lattice oxygen [40]. The local structures of LLO114 and LLO114-Y are probed by Raman spectra, which is sensitive to the short-range orderings. Figure S6 shows the spectra of the pristine LLO114 and LLO114-Y, which possesses typical Raman vibration features of LLOs. The peaks approximately at 595 and 475 cm^{-1} correspond to M–O (A_{1g}) and O–M–O bending (E_g) vibrational modes of the layered (R-3 m) phase. The peak about 425 cm^{-1} accompanied by other slight peaks (at 330 cm^{-1}, 545 cm^{-1}) repesents Li_2MnO_3 (C2/m) components [41]. Figure 5e, f analyses the Raman spectra of cycled samples via Raman peak fittings. An extra shoulder peak emerges at 631 cm^{-1}, which is assigned to TM-O vibration of spinel component, suggesting formation of spinel structure after the long cycles [42, 43]. The integrated intensity ratio of layered component to spinel component is used to quantify the structure

transformatnion (I_L:I_S). The value for LLO114-Y is 2.21, while that of LLO114 is only 1.23. The anlysis indicates that the layered structure is well maintained on LLO114-Y surface and significant spinel transformation occurs on LLO114 surface. The suppressed layered-to-spinel phase transformation in LLO114-Y is further proved by the HRTEM images. As shown in Fig. 5g, h, the fast Fourier transform (FFT) results exhibit that the surface region of LLO114 consists of a mixed phase (spinel-like phase and layered phases), while the surface region of LLO114-Y maintains well-layered structure. Line propfiles (white line) analyse the TM arrangement perpendicular to (001) plane. As shown in Fig. 5i, extra atomic peaks can be detected between two TM layers of LLO114 (marked by black arrows), indicating TM in Li layer at the particle surface. Figure S7 shows SEM images of LLO114 and LLO114-Y after long cycles. The spherical particles of LLO114 samples have been broken, while LLO114-Y sample is still intact. In addition, through the above tests, it is found that the LLO114 sample has a large degree of
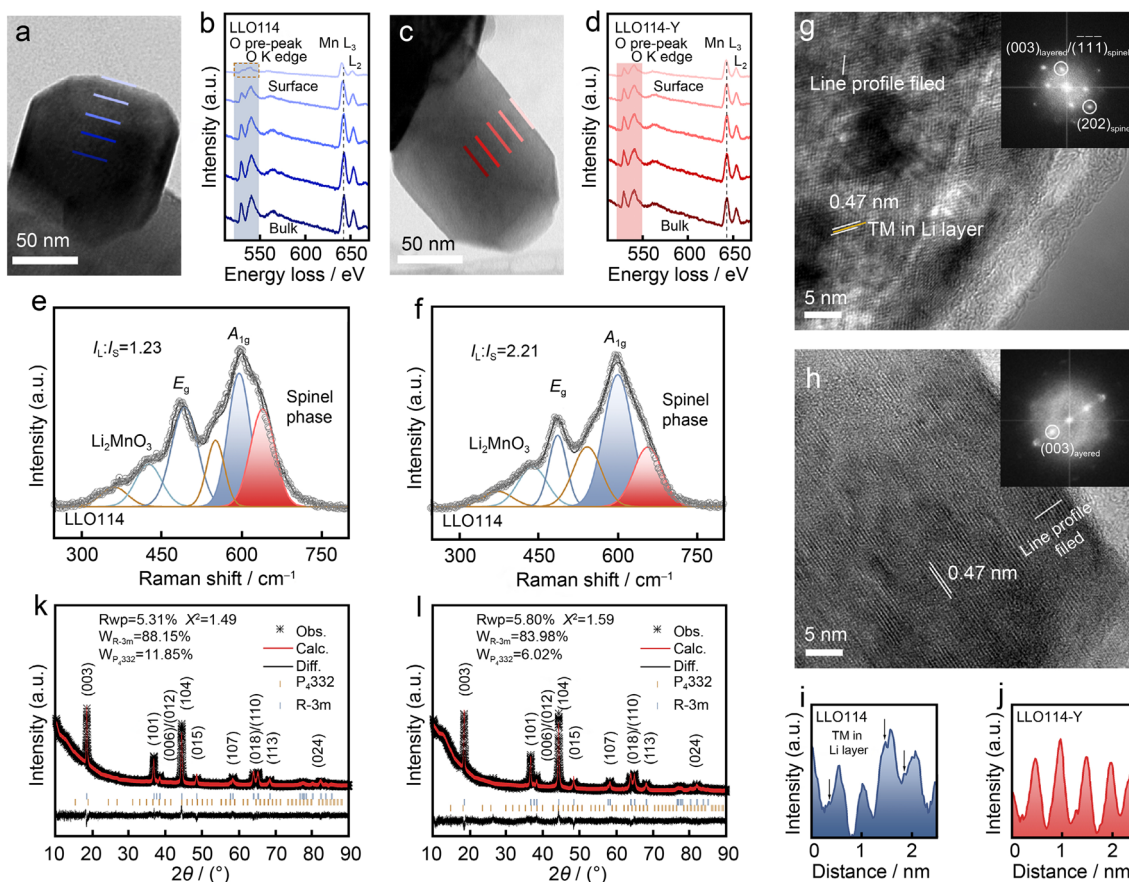
Fig. 5 **a**, **c** TEM image of a particle of the LLO114 and LLO114-Y, after cycles; **b**, **d** EELS spectrum profiles of LLO114 and LLO114-Y from the surface to the interior as marked by the solid lines with the same colour as in **a** and **c**; Raman spectra of **e** LLO114 and **f** LLO114-Y, after cycling; **g**, **h** HRTEM images of the LLO114 and LLO114-Y electrode materials after 140 cycles; **i**, **j** the related line intensity profile from edge to center, the black arrows in **i** indicate TM in Li layer; XRD patterns and two-phase refinement patterns for LLO114 **k** and LLO114-Y **l** after 140 cycles

primary particle phase transformation after a long cycle, which results in greater stress generated inside the secondary particles and ultimately leads to particle rupture [44]. XRD is used to analyse the global structural changes of the both samples after 140 cycles (Fig. 5k, l). Models of layered and spinel phases are used to fit the experiment patterns to quantify the bulk structure transformation (Table S3). The results show that the phase of spinel in cycled LLO114 reaches 11.85%, while the spinel phase of cycled LLO114-Y is 6.02%. The larger spinel structure transformation for LLO114 can be ascribed to diffusion of the oxygen vacancies into the bulk structure upon cycling, which causes cation migration. The above results demonstrate that the surface doping enhances structural stability of LLOs by reducing irreversible oxygen release. This is due to the fact that the bond strength of Y–O (714.1 ± 10.2 kJ·mol^{-1}) is stronger than that of Ni–O (366 ± 30.0 kJ·mol^{-1}), Co–O (397.4 ± 8.7 kJ·mol^{-1}) and Mn–O (362 ± 25.0 kJ·mol^{-1}). When the Y element is

doped on material surface, it is strong enough to prevent the surface O from escaping.

3.5 Electrochemical kinetic analysis

GITT is used to investigate more chemical diffusion coefficient of Li$^+$ ions. The values of Log(D/L^2) are used to represent the Li$^+$ diffusion coefficient, which can avoid misestimate due to the semblable size of two particles (Fig. S2), where D stands for Li$^+$ diffusion coefficient, and L for diffusion distance. The main difference between the two samples during the first cycle process is that LLO114 sample has a lower Li$^+$ diffusion coefficient at the end of discharge process in Fig. 6a. Anionic redox occurs in this region accompanied short-range atomic movements associated with the repeated oxygen-redox-driven migration of TM ions [45]. However, due to the existence of irreversible lattice oxygen redox in LLO114 sample, TMs migration also becomes irreversible resulting in reorganization of structure,
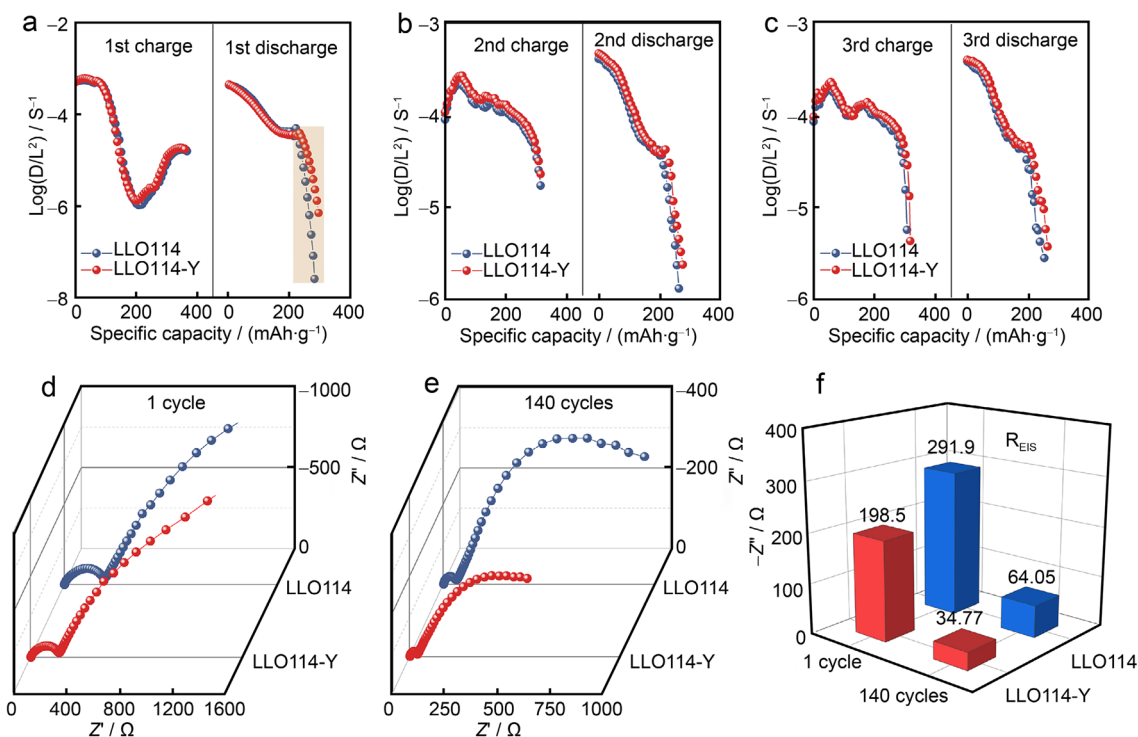
Fig. 6 Kinetics of LLO114 compared to LLO114-Y: **a–c** calculated Li$^+$ diffusion coefficients versus specific capacity for LLO114 and LLO114-Y in the 1st, 2nd and 3rd cycles, respectively; **d** EIS spectra for LLO114 and LLO114-Y in the initial discharge state and **e** in the discharge state after 140 cycles; **f** The R_{EIS} values of the two samples were compared after the first and 140th cycles

which blocks Li$^+$ diffusion channel [46, 47]. The Li$^+$ diffusion coefficient of LLO114-Y is larger than that of LLO114 sample in the second and third charge–discharge process (Fig. 6b, c). The discharge terminal of LLO114 sample continues to be slightly lower than that of LLO114-Y sample, indicating small structural changes continued during extent cycle.

Interfacial impedance could be affected by irreversible lattice oxygen release as well. Electrochemical impedance spectroscopy was used to show more detailed information about impedance changes. Figure 6d, e presents Nyquist plots and fitted plots of each electrode at discharged state after the first cycle and the 140th cycles. Typical of the EIS, spectra characteristics mainly consist of three parts [48]. The high-frequency region, the first semicircle, is related to the diffusion and migration of Li$^+$ through solid electrolyte interface film on the surface of active material particles. The second semicircle at high frequencies in Nyquist plot is related to the transport of electrons inside the active material particles. The low-frequency region is an oblique line associated with the solid diffusion process of Li$^+$ within the active material particles. However, due to the large charge transfer impedance in our data, Warburg impedance is not shown in the range of 10^5–10^{-2} Hz. LLO114 exhibits a higher contact impedance than LLO114-Y and similar charge transfer impedance in the first cycle (Fig. 6f). This is due to the

decomposition of electrolytes by reactive oxygen species, which release H$^+$, CO and CO$_2$, thus forming non-conductive solid electrolyte interphase (SEI) [49]. After cycles, LLO114-Y sample shows a smaller charge-transfer resistance compared to LLO114 sample, implying that catalytic side reactions at the interface between cathode and electrolyte are suppressed by stable surface oxygen framework.

4 Conclusion

In this work, on the basis of Hume-Rothery rule, element yttrium has been successfully in cooperated into the particle surface without diffusing into the bulk lattice in Li-rich layered oxide cathode Li$_{1.2}$Ni$_{0.13}$Co$_{0.13}$Mn$_{0.54}$O$_2$. Due to a strong bond with surface oxygen, this optimized surface dopant can suppress oxygen release, and has no any capacity fade. The suppressed oxygen release significantly reduces the formation of oxygen vacancies, preventing the structure degradation from surface extending to bulk. As a result, the sample with no oxygen loss exhibits less irreversible capacity loss and improved cycle performance. Postmortem analysis revealed that Y-doped sample still maintains well-layered structure even after 140 cycles. Electrochemical kinetic analysis shows that the Y-doped sample has better electrode kinetics and smaller polarization due to well-maintained 2D

Li$^+$ diffusion path and less charge transfer resistance. This strategy is expected to promote the developing progress of Li-rich layered oxide cathodes with high performances and also promises to open a door for simple implementation of surface doping.

Declarations

Conflict of interest The authors declare no conflict of interest.

References

1. Zeng XQ, Li M, Abd El-Hady D, Alshitari W, Al-Bogami AS, Lu J, Amine K. Commercialization of lithium battery technologies for electric vehicles. Adv Energy Mater. 2019;9(27):1900161.
2. Masias A, Marcicki J, Paxton WA. Opportunities and challenges of lithium ion batteries in automotive applications. Am Chem Soc Energy Lett. 2021;6(2):621.
3. Hu SJ, Pillai AS, Liang GM, Pang WK, Wang HQ, Li QY, Guo ZP. Li-rich layered oxides and their practical challenges: recent progress and perspectives. Electrochem Energy Rev. 2019;2(2):277.
4. Zheng HF, Han X, Guo WB, Lin L, Xie QS, Liu PF, He W, Wang LS, Peng DL. Recent developments and challenges of Li-rich Mn-based cathode materials for high-energy lithium-ion batteries. Mater Today Energy. 2020;18:2468.
5. He W, Guo W, Wu H, Lin L, Liu Q, Han X, Xie Q, Liu P, Zheng H, Wang L, Yu X, Peng DL. Challenges and recent advances in high capacity Li-rich cathode materials for high energy density lithium-ion batteries. Adv Mater. 2021;33(50):2005937.
6. Sharifi-Asl S, Lu J, Amine K, Shahbazian-Yassar R. Oxygen release degradation in Li-ion battery cathode materials: mechanisms and mitigating approaches. Adv Energy Mater. 2019;9(22):1900551.
7. Lei Y, Ni J, Hu Z, Wang Z, Gui F, Li B, Ming P, Zhang C, Elias Y, Aurbach D, Xiao Q. Surface modification of Li-rich Mn-based layered oxide cathodes: challenges, materials, methods, and characterization. Adv Energy Mater. 2020;10(41):2002506.
8. Fan YM, Zhang WC, Zhao YL, Guo ZP, Cai Q. Fundamental understanding and practical challenges of lithium-rich oxide cathode materials: layered and disordered-rocksalt structure. Energy Storage Mater. 2021;40:2405.
9. Lu ZH, Dahn JR. Understanding the anomalous capacity of Li/Li[Ni$_x$Li$_{(1/3-2x/3)}$ Mn$_{(2/3-x/3)}$]O$_2$ cells using in situ X-ray diffraction and electrochemical studies. J Electrochem Soc. 2002;149(7):A815.
10. Armstrong AR, Holzapfel M, Novák P, Johnson CS, Kang SH, Thackeray MM, Bruce PG. Demonstrating oxygen loss and associated structural reorganization in the lithium battery cathode Li[Ni$_{0.2}$Li$_{0.2}$Mn$_{0.6}$]O$_2$. J Am Chem Soc. 2006;128:8694.
11. Luo K, Roberts MR, Hao R, Guerrini N, Pickup DM, Liu YS, Edstrom K, Guo J, Chadwick AV, Duda LC, Bruce PG. Charge-compensation in 3d-transition-metal-oxide intercalation cathodes through the generation of localized electron holes on oxygen. Nat Chem. 2016;8(7):684.
12. Csernica PM, Kalirai SS, Gent WE, Lim K, Yu YS, Liu Y, Ahn SJ, Kaeli E, Xu X, Stone KH, Marshall AF, Sinclair R, Shapiro DA, Toney MF, Chueh WC. Persistent and partially mobile oxygen vacancies in Li-rich layered oxides. Nat Energy. 2021;6(6):642.
13. Yan P, Zheng J, Tang ZK, Devaraj A, Chen G, Amine K, Zhang JG, Liu LM, Wang C. Injection of oxygen vacancies in the bulk lattice of layered cathodes. Nat Nanotechnol. 2019;14(6):602.
14. Hu E, Yu X, Lin R, Bi X, Lu J, Bak S, Nam K-W, Xin HL, Jaye C, Fischer DA, Amine K, Yang XQ. Evolution of redox couples in Li- and Mn-rich cathode materials and mitigation of voltage fade by reducing oxygen release. Nat Energy. 2018;3(8):690.
15. Yin C, Wen XH, Wan LY, Shi ZP, Wei ZN, Li X, Gu QW, Qiu B, Liu ZP. Surface reinforcement doping to suppress oxygen release of Li-rich layered oxides. J Power Sources. 2021;503:2100552.
16. Liu S, Liu Z, Shen X, Li W, Gao Y, Banis MN, Li M, Chen K, Zhu L, Yu R, Wang Z, Sun X, Lu G, Kong Q, Bai X, Chen L. Surface doping to enhance structural integrity and performance of Li-rich layered oxide. Adv Energy Mater. 2018;8(31):1802105.
17. Lee Y, Shin J, Kang H, Lee D, Kim TH, Kwon YK, Cho E. Promoting the reversible oxygen redox reaction of Li-excess layered cathode materials with surface vanadium cation doping. Adv Sci. 2021;8(6):2003013.
18. He W, Liu PF, Zhang YG, Lin J, Qu BH, Zheng ZM, Wang J, Zhang YM, Sa BS, Wang LS, Xie QS, Peng DL. Utilizing the different distribution habit of La and Zr in Li-rich Mn-based cathode to achieve fast lithium-ion diffusion kinetics. J Power Sources. 2021;499:378.
19. Bao WD, Qian GN, Zhao LQ, Yu Y, Su LX, Cai XC, Zhao HJ, Zuo YQ, Zhang Y, Li HY, Peng ZJ, Xie J. Simultaneous enhancement of interfacial stability and kinetics of single-crystal LiNi$_{0.6}$Mn$_{0.2}$Co$_{0.2}$O$_2$ through optimized surface coating and doping. Nano Lett. 2020;20(12):8832.
20. Fabris S, Elsässer C. First-principles analysis of cation segregation at grain boundaries in α-Al$_2$O$_3$. Acta Mater. 2003;51(1):71.
21. Gong MM, Dey S, Wu LJ, Chang CH, Li H, Castro RHR, Liu F. Effects of concurrent grain boundary and surface segregation on the final stage of sintering: the case of lanthanum doped yttria-stabilized zirconia. J Mater Sci Technol. 2017;33(3):251.
22. Yang C, Feng B, Wei J, Tochigi E, Ishihara S, Shibata N, Ikuhara Y. Atomic and electronic band structures of Ti-doped Al$_2$O$_3$ grain boundaries. Acta Mater. 2020;201:488.
23. Lackner P, Brandt AJ, Diebold U, Schmid M. Few-monolayer yttria-doped zirconia films: segregation and phase stabilization. J Chem Phys. 2020;152(6): 064709.
24. Geng C, Rathore D, Heino D, Zhang N, Hamam I, Zaker N, Botton GA, Omessi R, Phattharasupakun N, Bond T, Yang C, Dahn JR. Mechanism of action of the tungsten dopant in LiNiO$_2$ positive electrode materials. Adv Energy Mater. 2021;12(6):2103067.
25. Li N, An R, Su YF, Wu F, Bao LY, Chen L, Zheng Y, Shou HF, Chen S. The role of yttrium content in improving electrochemical performance of layered lithium-rich cathode materials for Li-ion batteries. J Mater Chem A. 2013;1(34):9760.
26. Zhao XX, Liang GC, Liu H, Liu YY. Improved conductivity and electrochemical properties of LiNi$_{0.5}$Co$_{0.2}$Mn$_{0.3}$O$_2$ materials via yttrium doping. R Soc Chem Adv. 2018;8(8):4142.
27. Li L, Chang YL, Xia H, Song BH, Yang JR, Lee KS, Lu L. NH$_4$F surface modification of Li-rich layered cathode materials. Solid State Ionics. 2014;264:36.
28. Li L, Song BH, Chang YL, Xia H, Yang JR, Lee KS, Lu L. Retarded phase transition by fluorine doping in Li-rich layered

$Li_{12}Mn_{0.54}Ni_{0.13}Co_{0.13}O_2$ cathode material. J Power Sources. 2015;283:162.

29. Mangalaraja RV, Mouzon J, Hedström P, Kero I, Ramam KVS, Camurri CP, Odén M. Combustion synthesis of Y_2O_3 and Yb–Y_2O_3. J Mater Process Technol. 2008;208(1–3):415.

30. Han JT, Zheng HF, Hu ZY, Luo XR, Ma YT, Xie QS, Peng DL, Yue GH. Facile synthesis of Li-rich layered oxides with spinel-structure decoration as high-rate cathode for lithium-ion batteries. Electrochim Acta. 2019;299:844.

31. Huang C, Wang ZJ, Fang ZQ, Zhao SX, Ci LJ. Achieving high initial coulombic efficiency and low voltage dropping in Li-rich Mn-based cathode materials by metal-organic frameworks-derived coating. J Power Sources. 2021;499:378.

32. Chong SK, Wu YF, Chen YZ, Guo SW, Tai ZG, Shu CY, Tan Q, Sun JJ, Liu YN. Mn-based layered oxide microspheres assembled by ultrathin nanosheets as cathode material for potassium-ion batteries. Electrochim Acta. 2019;293:299.

33. Yang J, Chen Y, Li Y, Xi X, Zheng J, Zhu Y, Xiong Y, Liu S. Encouraging voltage stability upon long cycling of Li-rich Mn-based cathode materials by Ta-Mo dual doping. Am Chem Soc Appl Mater Interfaces. 2021;13(22):25981.

34. Zhang PP, Zhai XH, Huang H, Zhou JF, Li XB, He YP, Guo ZC. Suppression of structural phase transformation of Li-rich Mn-based layered cathode materials with Na ion substitution strategy. Electrochim Acta. 2020;349:13.

35. Li SM, Bai L, Shi HB, Hao XF, Chen L, Ma ZP, Qin XJ, Shao GJ. Coral-like Prussian blue analogues-derived bimetallic phosphide with enhanced electrocatalytic performance for hydrogen evolution reaction. Int J Hydrogen Energy. 2021;46(55):27883.

36. Freunberger SA, Chen Y, Peng Z, Griffin JM, Hardwick LJ, Barde F, Novak P, Bruce PG. Reactions in the rechargeable lithium-O_2 battery with alkyl carbonate electrolytes. J Am Chem Soc. 2011;133(20):8040.

37. Renfrew SE, McCloskey BD. Residual lithium carbonate predominantly accounts for first cycle CO_2 and CO outgassing of Li-stoichiometric and Li-rich layered transition-metal oxides. J Am Chem Soc. 2017;139(49):17853.

38. Qiu B, Zhang M, Wu L, Wang J, Xia Y, Qian D, Liu H, Hy S, Chen Y, An K, Zhu Y, Liu Z, Meng YS. Gas-solid interfacial modification of oxygen activity in layered oxide cathodes for lithium-ion batteries. Nat Commun. 2016;7:12108.

39. Qian D, Xu B, Chi M, Meng YS. Uncovering the roles of oxygen vacancies in cation migration in lithium excess layered oxides. Phys Chem Chem Phys. 2014;16(28):14665.

40. Guo HC, Wei Z, Jia K, Qiu B, Yin C, Meng FQ, Zhang QH, Gu L, Han SJ, Liu Y, Zhao H, Jiang W, Cui HF, Xia YG, Liu ZP. Abundant nanoscale defects to eliminate voltage decay in Li-rich cathode materials. Energy Storage Mater. 2019;16:220.

41. Yu DY, Yanagida K. Structural analysis of Li_2MnO_3 and related Li-Mn-O materials. J Electrochem Soc. 2011;158(9):1015.

42. Venkateswara Rao C, Soler J, Katiyar R, Shojan J, West WC, Katiyar RS. Investigations on electrochemical behavior and structural stability of $Li_{1.2}Mn_{0.54}Ni_{0.13}Co_{0.13}O_2$ lithium-ion cathodes via in-citu and ex-citu Raman spectroscopy. J Phys Chem C. 2014;118(26):14133.

43. Zheng Y, Chen L, Su YF, Tan J, Bao LY, Lu Y, Wang J, Chen RJ, Chen S, Wu F. An interfacial framework for breaking through the Li-ion transport barrier of Li-rich layered cathode materials. J Mater Chem A. 2017;5(46):24292.

44. Aishova A, Park GT, Yoon CS, Sun YK. Cobalt-free high-capacity Ni-rich layered $Li[Ni_{0.9}Mn_{0.1}]O_2$ Cathode. Adv Energy Mater. 2019;10(4):1903179.

45. Assat G, Tarascon JM. Fundamental understanding and practical challenges of anionic redox activity in Li-ion batteries. Nat Energy. 2018;3(5):373.

46. Zheng J, Gu M, Xiao J, Zuo P, Wang C, Zhang JG. Corrosion/fragmentation of layered composite cathode and related capacity/voltage fading during cycling process. Nano Lett. 2013;13(8):3824.

47. Zuo W, Liu X, Qiu J, Zhang D, Xiao Z, Xie J, Ren F, Wang J, Li Y, Ortiz GF, Wen W, Wu S, Wang MS, Fu R, Yang Y. Engineering Na^+-layer spacings to stabilize Mn-based layered cathodes for sodium-ion batteries. Nat Commun. 2021;12(1):4903.

48. Wang S, Zhang J, Gharbi O, Vivier V, Gao M, Orazem ME. Electrochemical impedance spectroscopy. Nat Rev Methods Primers. 2021;1(1):42.

49. Zhang XD, Shi JL, Liang JY, Yin YX, Zhang JN, Yu XQ, Guo YG. Suppressing surface lattice oxygen release of Li-rich cathode materials via heterostructured spinel $Li_4Mn_5O_{12}$ coating. Adv Mater. 2018;30:1801751.